EUROPEAN ORGANISATION FOR NUCLEAR RESEARCH (CERN)

Submitted to: PRC

CERN-EP-2023-001
February 9, 2023

Measurements of the suppression and correlations of dijets in Xe+Xe collisions at $\sqrt{s_{NN}}$ = 5.44 TeV

The ATLAS Collaboration

Measurements of the suppression and correlations of dijets is performed using 3 μb^{-1} of Xe+Xe data at $\sqrt{s_{\mathrm{NN}}}$ = 5.44 TeV collected with the ATLAS detector at the LHC. Dijets with jets reconstructed using the R = 0.4 anti-k_t algorithm are measured differentially in jet p_{T} over the range of 32 GeV to 398 GeV and the centrality of the collisions. Significant dijet momentum imbalance is found in the most central Xe+Xe collisions, which decreases in more peripheral collisions. Results from the measurement of per-pair normalized and absolutely normalized dijet p_{T} balance are compared with previous Pb+Pb measurements at $\sqrt{s_{\mathrm{NN}}}$ = 5.02 TeV. The differences between the dijet suppression in Xe+Xe and Pb+Pb are further quantified by the ratio of pair nuclear-modification factors. The results are found to be consistent with those measured in Pb+Pb data when compared in classes of the same event activity and when taking into account the difference between the center-of-mass energies of the initial parton scattering process in Xe+Xe and Pb+Pb collisions. These results should provide input for a better understanding of the role of energy density, system size, path length, and fluctuations in the parton energy loss.

Contents

1 Introduction

A major focus of relativistic heavy-ion physics is to study the quark-gluon plasma (QGP), a hot and dense medium composed of deconfined quarks and gluons. During the initial stages of heavy-ion collisions, hard-scattering interactions between constituents of incoming nuclei may occur. In leading-order calculations in perturbative quantum chromodynamics, two high transverse momenta (p_{T}) partons (quarks and/or gluons) are produced in these interactions. These partons then fragment and hadronize to form two jets that are oriented back-to-back in azimuth. When traversing the QGP, these jets suffer radiative and collisional energy loss leading to a phenomenon known as jet quenching [1, 2]. Jet quenching has been observed and quantified in many measurements at RHIC and the LHC (for a recent review see Ref. [3]), but the theoretical understanding of partonic interactions and properties of the QGP is still incomplete.

A basic observable quantifying the impact of jet quenching on inclusive jets is the jet nuclear-modification factor, R_{AA} [4–6]. A factor of two suppression of inclusive jet production in central Pb+Pb collisions compared to the production in pp collisions is seen in measurements of R_{AA}. While measurements of inclusive jet suppression contain contributions from jets traversing different path lengths in the QGP and suffering differently from jet quenching fluctuations, the measurements of dijets provide additional information about the path-length dependence of the energy loss and the role of fluctuations in the energy loss [7, 8]. Dijet suppression in Pb+Pb collisions was measured in terms of the momentum balance [9–13] and the pair nuclear-modification factor [13], which quantified the differences between the suppression of the leading (in transverse momentum) jet and the subleading jet (opposite in azimuth).

So far, only inclusive charged-hadron suppression was measured in Xe+Xe collisions [14–16], while the parton energy-loss measurements involving jets and dijets at the LHC have only been performed in Pb+Pb collisions. The 2017 LHC Xe+Xe run provides a possibility to study jet quenching in collisions of nuclei lighter than Pb, which is attractive for several reasons. First, the underlying event (UE) in the most central collisions, where the collision geometry is the most symmetric, is smaller in Xe+Xe collisions than in Pb+Pb collisions. Secondly, the decrease in the number of nucleons or the nuclear radius between Pb and Xe nuclei may affect the amount of jet quenching through a reduction in both the overall energy density and

the path lengths traversed by the hard-scattered partons in the medium. Consequently, measurements of dijets in different collision systems should further constrain the impact of the path length, energy density, and fluctuations on the jet quenching. Studying the parton energy loss in a collision system that is smaller than the Pb+Pb system may also help to predict the energy loss for oxygen–oxygen collisions, which are intended to be performed during LHC Run 3 [17]. This paper reports the first measurement of jet suppression for Xe+Xe collisions.

The analysis presented here follows closely the techniques that were used to measure dijets in Pb+Pb collisions [13]. The highest p_{T} jet in the event, the leading jet, and the second highest p_{T} jet, the subleading jet are studied. The leading jet transverse momentum, $p_{\mathrm{T},1}$ is required to be greater than 100 GeV and the subleading jet transverse momentum, $p_{\mathrm{T},2}$, greater than 32 GeV. Both the jets are required to be in the rapidity[1] region $|y| < 2.1$. The subleading jet is required to be on the opposite side in azimuth from the leading jet, which is defined by the condition $\Delta\phi = |\phi_1 - \phi_2| > 7\pi/8$. The momentum balance between the leading and subleading jet is quantified by the ratio

$$x_{\mathrm{J}} = \frac{p_{\mathrm{T},2}}{p_{\mathrm{T},1}}.$$

The distribution of x_{J} can be normalized by the number of dijets (N_{pair}),

$$\frac{1}{N_{\mathrm{pair}}}\frac{\mathrm{d}N_{\mathrm{pair}}}{\mathrm{d}x_{\mathrm{J}}}, \tag{1}$$

which is called *per-pair normalized* momentum-imbalance distribution. Alternatively, the distribution can be normalized by the effective heavy-ion luminosity,

$$\frac{1}{N_{\mathrm{evt}}}\frac{1}{\langle T_{\mathrm{AA}}\rangle}\frac{\mathrm{d}N_{\mathrm{pair}}}{\mathrm{d}x_{\mathrm{J}}}, \tag{2}$$

which is called the *absolutely normalized* momentum-imbalance distribution, where $\langle T_{\mathrm{AA}}\rangle$ is the average nuclear-thickness function and N_{evt} is the number of minimum bias events in a given centrality interval. The absolutely normalized momentum-imbalance distribution allows the differences between the yields of dijets with a given dijet momentum-imbalance in different collision centrality intervals to be directly quantified. Both the per-pair normalized and absolutely normalized dijet momentum-imbalance distributions were previously measured in Pb+Pb collisions [13]. The dijet yields in Xe+Xe collisions are also extracted to calculate the pair nuclear-modification factors for leading and subleading jets. Measurements made in Xe+Xe collisions are compared with those obtained for Pb+Pb collisions.

2 ATLAS detector and trigger

The ATLAS detector [18] at the LHC covers nearly the full solid angle around the nominal interaction point. It contains an inner tracking detector (ID) surrounded by a thin superconducting solenoid, electromagnetic

[1] ATLAS uses a right-handed coordinate system with its origin at the nominal interaction point (IP) in the center of the detector and the z-axis along the beam pipe. The x-axis points from the IP to the center of the LHC ring, and the y-axis points upward. Cylindrical coordinates (r, ϕ) are used in the transverse plane, ϕ being the azimuthal angle around the z-axis. The pseudorapidity is defined in terms of the polar angle θ as $\eta = -\ln\tan(\theta/2)$ and the rapidity is defined in terms of the energy E and z-component of the momentum, p_z, as $y = 1/2\ln((E + p_z)/(E - p_z))$. Transverse momentum and transverse energy are defined as $p_{\mathrm{T}} = p\sin(\theta)$ and $E_{\mathrm{T}} = E\sin(\theta)$, respectively. The angular distance between two objects with relative differences $\Delta\eta$ in pseudorapidity and $\Delta\phi$ in azimuth is given by $\Delta R = \sqrt{(\Delta\eta)^2 + (\Delta\phi)^2}$.

and hadronic calorimeters, a zero-degree calorimeter, and a muon spectrometer that incorporates three large superconducting toroidal magnets. The inner-detector system is immersed in a 2 T axial magnetic field and provides charged-particle tracking in the range of $|\eta| < 2.5$ with 2π coverage in azimuth. The ATLAS calorimeter system covers the pseudorapidity range of $|\eta| < 4.9$. In the region of $|\eta| < 3.2$, the electromagnetic calorimetry is provided by both barrel and endcap high-granularity lead/liquid-argon (LAr) calorimeters, with an additional thin LAr presampler covering $|\eta| < 1.8$, to enable corrections for energy lost in material upstream of the calorimeters. Hadronic calorimetry is provided by a steel/scintillating-tile calorimeter that is segmented into three barrel structures with $|\eta| < 1.7$, and two copper/LAr hadronic endcap calorimeters. To complete the solid angle coverage, forward ($3.2 < |\eta| < 4.9$) copper/LAr and tungsten/LAr calorimeter modules (FCal) are used, optimized for electromagnetic and hadronic measurements, respectively.

Data are recorded with a multi-stage trigger system [19]. Events are selected using hardware-based first-level triggers (L1) implemented in custom-electronics, and then processed by a high-level trigger (HLT) to further reduce the accepted event rate and provide additional purity.

An extensive software suite [20] is used in data simulation, in the reconstruction and analysis of real and simulated data, in detector operations, and in the trigger and data acquisition systems of the experiment.

3 Data selection and Monte Carlo simulation samples

The analysis uses data from ^{129}Xe+^{129}Xe collisions at $\sqrt{s_{\mathrm{NN}}} = 5.44$ TeV collected in 2017 at the LHC with a total integrated luminosity of 3 $\mu\mathrm{b}^{-1}$. Events were recorded using a combination of two triggers designed to select minimum-bias (MB) collisions, which allows measured jets to be reconstructed with full efficiency. These triggers require the total transverse energy deposited in the calorimeters at L1 to be more than 4 GeV or if the total transverse energy at L1 is less than 4 GeV then the presence of at least one track reconstructed in the ID is required.

In addition to the trigger selections, events are required to have a reconstructed primary vertex and satisfy criteria that ensure stable detector conditions. A few recorded events ($\approx 0.1\%$) consistent with two Xe+Xe interactions in the same bunch crossing (pileup) are removed based on the tight correlation between the sum of the total transverse energy in the forward calorimeter ($\Sigma E_{\mathrm{T}}^{\mathrm{FCal}}$) and the number of reconstructed tracks matched to the primary vertex.

The level of overall event activity or "centrality", which is indicative of the degree of overlap between the two colliding nuclei, is characterized using $\Sigma E_{\mathrm{T}}^{\mathrm{FCal}}$ measured at the electromagnetic scale [21]. The Glauber model [22] is used to obtain a correspondence between the $\Sigma E_{\mathrm{T}}^{\mathrm{FCal}}$ distribution and the fraction of the total inelastic Xe+Xe cross-section, allowing the setting of the centrality percentiles [23, 24]. A Glauber Model analysis was also applied to relate quantiles of the $\Sigma E_{\mathrm{T}}^{\mathrm{FCal}}$ distribution to geometric properties of the collision such as $\langle T_{\mathrm{AA}} \rangle$. Centrality intervals in Xe+Xe collisions used in the analysis along with $\langle T_{\mathrm{AA}} \rangle$ are summarized in Table 1. The comparison of Xe+Xe and Pb+Pb results is performed in the same centrality intervals, covering the centrality range 0–80% as listed in Table 1. In addition, the results for both systems are also compared by selecting events with similar activity, quantified by $\Sigma E_{\mathrm{T}}^{\mathrm{FCal}}$. For this comparison, events in Xe+Xe collisions are selected in intervals of $\Sigma E_{\mathrm{T}}^{\mathrm{FCal}}$ matching the $\Sigma E_{\mathrm{T}}^{\mathrm{FCal}}$ intervals in Pb+Pb collisions that correspond to the Pb+Pb centrality intervals of 10–20%, 20–40% and 40–60% used in Ref. [13]. The corresponding Xe+Xe centrality intervals are summarized in Table 2.

Table 1: The centrality intervals in Xe+Xe collisions and their corresponding $\langle T_{\mathrm{AA}} \rangle$ values with their respective absolute uncertainties.

Centrality	$\langle T_{\mathrm{AA}}^{\mathrm{Xe+Xe}} \rangle$ [mb^{-1}]
0–10%	12.38±0.08
10–20%	7.53±0.09
20–40%	3.52±0.09
40–80%	0.630±0.036

Table 2: The centrality intervals in Xe+Xe and Pb+Pb collisions for matching $\Sigma E_{\mathrm{T}}^{\mathrm{FCal}}$ intervals and respective $\langle T_{\mathrm{AA}} \rangle$ values for Xe+Xe collisions.

Xe+Xe Cent.	Pb+Pb Cent.	$\langle T_{\mathrm{AA}}^{\mathrm{Xe+Xe}} \rangle$ [mb^{-1}]	$\Sigma E_{\mathrm{T}}^{\mathrm{FCal}}$ [TeV]
0–7.7%	10–20%	13.05±0.08	2.06–3.00
7.7–29.9%	20–40%	6.45±0.09	0.89–2.06
29.9–53.2%	40–60%	1.81±0.07	0.30–0.89

Monte Carlo (MC) simulations are used to understand the performance of the ATLAS detector in high occupancy Xe+Xe data samples and to correct the data for detector effects. A sample of 9×10^6 pp jet events was generated using Pythia 8 [25] at $\sqrt{s} = 5.44$ TeV with the A14 set of tuned parameters [26] and the NNPDF23LO parton distribution functions [27]. To correctly describe the UE of Xe+Xe collisions, these generated MC events were overlaid onto events from a dedicated sample of minimum-bias Xe+Xe data. The detector response was simulated [20] using Geant4 [28, 29]. A pp MC sample of 2.4×10^6 jet events with the same settings but at $\sqrt{s} = 5.02$ TeV was also generated to determine the correction for the difference between the center-of-mass energies in Xe+Xe and Pb+Pb collisions. In addition, samples of jet events using Herwig++ [30] with the UEEE5 tune [31] and the CTEQ6L1 parton distribution functions [32] were generated to assess systematic uncertainties.

4 Jet reconstruction

The jet reconstruction procedure follows that used by ATLAS for previous jet measurements in Pb+Pb collisions described in Ref. [33], including the UE subtraction procedure. Jets are reconstructed using the anti-k_t algorithm [34] with radius parameter $R = 0.4$ implemented in the `FastJet` software package [35]. Jets are formed by clustering calorimetric towers of angular size $\Delta\eta \times \Delta\phi = 0.1 \times \pi/32$. The energy in the tower is obtained by summing the energies deposited in calorimeter cells at the electromagnetic energy scale within the tower boundaries. An η- and ϕ-dependent UE subtraction is performed for each calorimeter tower within the jet using an iterative procedure, where the background due to the UE is modulated to account for the effects of hydrodynamic flow [36]. Then, jet η and p_{T} dependent correction factors derived from simulations are applied to the measured jet energy to correct for the calorimeter energy response [37]. This calibration is followed by a cross-calibration that relates the jet energy scale of jets reconstructed by the procedure outlined above to the jet energy scale in 13 TeVpp collisions [38]. An additional correction based on in situ studies of jets recoiling against photons, Z bosons, and jets in other regions of the calorimeters is applied [39].

Jets are defined at the generator level in the MC sample before detector simulation by applying the anti-k_t

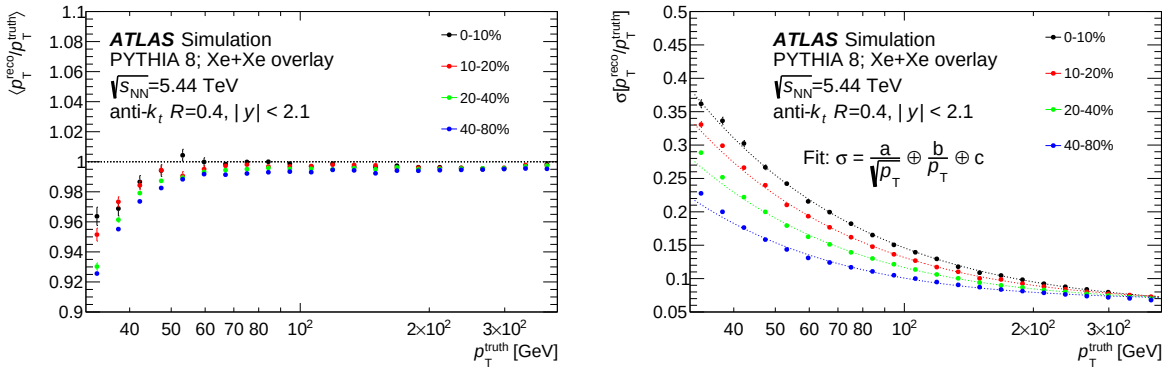

Figure 1: The performance of (left) the JES and (right) the JER for jets with $|y| < 2.1$ evaluated as a function of $p_{\mathrm{T}}^{\mathrm{truth}}$ in different centrality bins. The right plot includes JER fits shown with dashed curves (for details, see the text). Simulated hard scatter events were overlaid onto events from a dedicated sample of minimum-bias Xe+Xe data.

algorithm with $R = 0.4$ to stable particles with a proper lifetime greater than 30 ps, but excluding muons and neutrinos, which do not leave significant energy deposits in the calorimeter. After the detector simulation, the generator-level jets are matched to the nearest reconstructed jet within $\Delta R = 0.4$.

The performance of the jet reconstruction is shown in Figure 1 in terms of the jet energy scale (JES) and jet energy resolution (JER), which correspond to the mean and width of the jet response ($p_{\mathrm{T}}^{\mathrm{reco}}/p_{\mathrm{T}}^{\mathrm{truth}}$), where $p_{\mathrm{T}}^{\mathrm{reco}}$ and $p_{\mathrm{T}}^{\mathrm{truth}}$ are the reconstructed and generator level jet transverse momenta, respectively. The maximum departure of the JES from unity in the inclusive jet sample is 8% in peripheral collisions (40–80% centrality) for $p_{\mathrm{T}}^{\mathrm{truth}} < 50$ GeV. For $p_{\mathrm{T}}^{\mathrm{truth}} > 50$ GeV the JES is consistent with unity within 1%. A similar performance of the JES is seen in Pb+Pb collisions [13]. Contributions to the JER can be factorized into three terms, $\frac{a}{\sqrt{p_{\mathrm{T}}}} \oplus \frac{b}{p_{\mathrm{T}}} \oplus c$, where the constants a, b, and c quantify the magnitude of stochastic term, noise term, and constant term, respectively. The stochastic and constant terms are related to the calorimeter response to the showering process while the noise term constitutes the centrality-dependent part of JER that is driven by the p_{T}-independent UE fluctuations [40]. The JER is largest in 0–10% central collisions where $b = 11.3 \pm 0.1$ GeV, which is about 3 GeV smaller than the value of b in 0–10% central Pb+Pb collisions but similar to the value of b in 10–20% central Pb+Pb collisions [4]. Constants a and c are found to be consistent between Xe+Xe and Pb+Pb collisions. The impact of the small departure of the JES from unity on measured quantities and the impact of the JER is corrected for by the unfolding procedure.

5 Data analysis

The analysis is performed using the same methods as described in Ref. [13]. Jet pairs are formed from the two highest-p_{T} jets in the event. Jet pairs not fulfilling the selection criteria for leading and subleading jet defined in Section 1 are not used.

The distributions of dijet momentum-imbalance and the pair nuclear-modification factor are not calculated directly. They are obtained in the final step of the analysis from two-dimensional $(p_{\mathrm{T},1}, p_{\mathrm{T},2})$ distributions. The binning of $(p_{\mathrm{T},1}, p_{\mathrm{T},2})$ distributions follows a logarithmic distribution with 32 intervals between $p_{\mathrm{T}} = 10$ GeV and $p_{\mathrm{T}} = 398$ GeV. This binning allows the same intervals to be selected as those used in the previous dijet and inclusive jet measurements in Pb+Pb collisions [4, 13]. Distributions are measured in the p_{T} range of $32 - 398$ GeV. Bins with $p_{\mathrm{T}} < 32$ GeV are only used in MC simulation as underflow bins

in the unfolding procedure. The maximum value of 398 GeV is determined by the absence of jets with $p_{\mathrm{T}} > 398$ GeV in the data. In total, 14 325 dijets were analyzed in the full centrality range 0 – 80%.

The $(p_{\mathrm{T},1}, p_{\mathrm{T},2})$ distributions are corrected for the background from jet pairs not originating in the same hard process and from spurious jets from fluctuations of the UE. This combinatoric background is estimated from the data using the yield of dijets with angular separation $1.0 < \Delta\phi < 1.4$ from the leading jet. This angular requirement minimizes the contribution from real dijets, which have a maximum at $\Delta\phi = \pi$, and contributions from split jets in the vicinity of $\Delta\phi \approx 0.4$. The background jet yield is then subtracted from the yield of dijets with $\Delta\phi > 7\pi/8$. This correction is largest in the most central collisions and at low p_{T}. In the 0–10% centrality region, for $p_{\mathrm{T},1} > 100$ GeV and $32 < p_{\mathrm{T},2} < 50$ GeV, it subtracts up to 15% of the dijets while for all other p_{T} and centrality bins the correction subtracts less than 4% of the dijets. The presence of background jets may create a situation where such a jet has higher p_{T} than the real sub-leading jet. This background jet would then be falsely identified as the sub-leading jet and this would cause oversubtraction leading to inefficiency. The background-subtracted $(p_{\mathrm{T},1}, p_{\mathrm{T},2})$ distributions are corrected for this effect. The efficiency correction is estimated from the per-event rate of inclusive jets in data using the same procedure as described in Ref. [12]. After the background of size B is subtracted from the raw yields N^{raw}, the efficiency ϵ is applied using the formula: $N^{\mathrm{corr}} = (N^{\mathrm{raw}} - B)/\epsilon$, where N^{corr} is the final yield that goes into the unfolding. The efficiency correction is largest in the most central collisions at the lowest $p_{\mathrm{T},2}$ values, where it reaches 3%. For subleading jets with $p_{\mathrm{T},2} > 50$ GeV the efficiency correction is smaller than 1%.

After the combinatoric background-subtraction and efficiency correction, the $(p_{\mathrm{T},1}, p_{\mathrm{T},2})$ distributions are unfolded for the detector response using the Bayesian unfolding implemented in the `RooUnfold` package [41, 42]. The four-dimensional response matrices are filled symmetrically in reconstruction- and generator-level $(p_{\mathrm{T},1}, p_{\mathrm{T},2})$ to include the possibility that the leading and subleading jets are swapped due to resolution effects. Generator-level jets entering the response matrix satisfy the same y and $\Delta\phi$ conditions, but extend the minimum p_{T} to lower values ($p_{\mathrm{T},1} > 20$ GeV and $p_{\mathrm{T},2} > 10$ GeV) to account for the migration of jets in and out of the kinematic fiducial region. The unfolding procedure also corrects the jet reconstruction inefficiency when the reconstructed jet pair is lost due to resolution effects but the corresponding generator-level jet pair exists. The response matrices are reweighted in generator-level, $(p_{\mathrm{T},1}, p_{\mathrm{T},2})$ by smooth ratios of the $(p_{\mathrm{T},1}, p_{\mathrm{T},2})$ distributions in data to those in the reconstructed MC sample such that the $(p_{\mathrm{T},1}, p_{\mathrm{T},2})$ distributions in the response matrices better represent those in the data.

The number of iterations in the unfolding is chosen to be three for all the centrality intervals, which optimizes the balance between the statistical uncertainty and systematic bias introduced by the shapes of the distributions used to construct the response matrix. The statistical uncertainty is estimated by performing 100 unfoldings where each bin in input data and each bin in the response matrix are varied separately according to their corresponding statistical uncertainties. The standard deviation of these is evaluated in each bin and used as the estimate of the statistical uncertainty. The two values, one from the statistical uncertainty in the data and one from the statistical uncertainty in the response matrix are summed in quadrature to obtain the total statistical uncertainty in the unfolded distributions.

The unfolded $(p_{\mathrm{T},1}, p_{\mathrm{T},2})$ distributions are used to calculate the resulting one-dimensional dijet momentum-imbalance distributions defined in Equations (1) and (2). The unfolded $(p_{\mathrm{T},1}, p_{\mathrm{T},2})$ is mapped to the region $p_{\mathrm{T},2} \leq p_{\mathrm{T},1}$ and diagonally sliced to project the x_{J} distribution as described in Ref. [13]. The x_{J} bin boundaries are defined by the previously discussed logarithmic binning in transverse momentum. The x_{J} distributions measured in Xe+Xe collisions can be directly compared with distributions measured in Pb+Pb collisions. This comparison may be affected by the difference between the cross-sections, due to the different center-of-mass energies of the initial hard process scattering, in Xe+Xe and Pb+Pb collisions.

To quantify this difference, the factor $C(x_J)$ is calculated as a ratio of PYTHIA 8 x_J distributions in 5.44 TeV pp collisions to the same quantity in simulated 5.02 TeV pp collisions,

$$C(x_J) = \frac{1/N \, \mathrm{d}N^{\mathrm{pair}}_{\mathrm{PYTHIA8}}(pp, 5.44 \text{ TeV})/\mathrm{d}x_J}{1/N \, \mathrm{d}N^{\mathrm{pair}}_{\mathrm{PYTHIA8}}(pp, 5.02 \text{ TeV})/\mathrm{d}x_J}. \tag{3}$$

The normalization N is N_{pair} and $N_{\mathrm{evt}}\langle T_{\mathrm{AA}}\rangle$ for per-pair normalized and absolutely normalized distributions, respectively. The $C(x_J)$ factor can be used to scale the x_J distributions measured in Pb+Pb data. For the absolutely normalized x_J distributions, the magnitude of $C(x_J)$ ranges from 1.25 at low x_J values to 1.15 at x_J values approaching unity. For per-pair normalized x_J distributions, the magnitude of $C(x_J)$ is consistent with unity and it is not applied on per-pair normalized x_J distributions.

The unfolded $(p_{\mathrm{T},1}, p_{\mathrm{T},2})$ distributions are also projected onto the $p_{\mathrm{T},1}$ and $p_{\mathrm{T},2}$ axes to construct the pair nuclear-modification factors for dijets as a function of the leading jet p_{T},

$$R^{\mathrm{pair}}_{\mathrm{AA}}(p_{\mathrm{T},1}) = \frac{\frac{1}{\langle T_{\mathrm{AA}}\rangle N^{\mathrm{AA}}_{\mathrm{evt}}} \int_{0.32\times p_{\mathrm{T},1}}^{p_{\mathrm{T},1}} \frac{\mathrm{d}^2 N^{\mathrm{pair}}(\mathrm{AA})}{\mathrm{d}p_{\mathrm{T},1}\mathrm{d}p_{\mathrm{T},2}} \mathrm{d}p_{\mathrm{T},2}}{\frac{1}{\mathcal{L}_{pp}} \int_{0.32\times p_{\mathrm{T},1}}^{p_{\mathrm{T},1}} \frac{\mathrm{d}^2 N^{\mathrm{pair}}(pp)}{\mathrm{d}p_{\mathrm{T},1}\mathrm{d}p_{\mathrm{T},2}} \mathrm{d}p_{\mathrm{T},2}},$$

and as a function of subleading jet p_{T},

$$R^{\mathrm{pair}}_{\mathrm{AA}}(p_{\mathrm{T},2}) = \frac{\frac{1}{\langle T_{\mathrm{AA}}\rangle N^{\mathrm{AA}}_{\mathrm{evt}}} \int_{p_{\mathrm{T},2}}^{p_{\mathrm{T},2}/0.32} \frac{\mathrm{d}^2 N^{\mathrm{pair}}(\mathrm{AA})}{\mathrm{d}p_{\mathrm{T},1}\mathrm{d}p_{\mathrm{T},2}} \mathrm{d}p_{\mathrm{T},1}}{\frac{1}{\mathcal{L}_{pp}} \int_{p_{\mathrm{T},2}}^{p_{\mathrm{T},2}/0.32} \frac{\mathrm{d}^2 N^{\mathrm{pair}}(pp)}{\mathrm{d}p_{\mathrm{T},1}\mathrm{d}p_{\mathrm{T},2}} \mathrm{d}p_{\mathrm{T},1}}. \tag{4}$$

Here $\mathcal{L}_{pp}$ is the integrated luminosity of pp collisions and the boundaries in the integrals are given by the measured minimum value of x_J.

To evaluate the differences between the dijet quenching in Xe+Xe and Pb+Pb collisions the ratio of pair nuclear-modification factors for the leading jet is defined as

$$\begin{aligned}
\rho_{\mathrm{Xe,Pb}}(p_{\mathrm{T},1}) &= \frac{R^{\mathrm{pair}}_{\mathrm{AA}}(p_{\mathrm{T},1})|_{\mathrm{Xe+Xe}}}{R^{\mathrm{pair}}_{\mathrm{AA}}(p_{\mathrm{T},1})|_{\mathrm{Pb+Pb}}} = \\
&= \frac{\frac{1}{\langle T^{\mathrm{Xe+Xe}}_{\mathrm{AA}}\rangle N^{\mathrm{Xe+Xe}}_{\mathrm{evt}}} \int_{0.32\times p_{\mathrm{T},1}}^{p_{\mathrm{T},1}} \frac{\mathrm{d}^2 N^{\mathrm{pair}}(\mathrm{Xe+Xe, 5.44\ TeV})}{\mathrm{d}p_{\mathrm{T},1}\mathrm{d}p_{\mathrm{T},2}} \mathrm{d}p_{\mathrm{T},2}}{C(p_{\mathrm{T},1}) \times \frac{1}{\langle T^{\mathrm{Pb+Pb}}_{\mathrm{AA}}\rangle N^{\mathrm{Pb+Pb}}_{\mathrm{evt}}} \int_{0.32\times p_{\mathrm{T},1}}^{p_{\mathrm{T},1}} \frac{\mathrm{d}^2 N^{\mathrm{pair}}(\mathrm{Pb+Pb, 5.02\ TeV})}{\mathrm{d}p_{\mathrm{T},1}\mathrm{d}p_{\mathrm{T},2}} \mathrm{d}p_{\mathrm{T},2}}.
\end{aligned}$$

As there is no reference pp data at 5.44 TeV, the factor $C(p_{\mathrm{T},1})$ is introduced to account for the difference between the center-of-mass energies of 5.44 TeV and 5.02 TeV collision data. It is evaluated using PYTHIA 8 Monte Carlo simulations as

$$C(p_{\mathrm{T},1}) = \frac{\int_{0.32\times p_{\mathrm{T},1}}^{p_{\mathrm{T},1}} \frac{\mathrm{d}^2 N^{\mathrm{pair}}_{\mathrm{PYTHIA8}}(pp, 5.44 \text{ TeV})}{\mathrm{d}p_{\mathrm{T},1}\mathrm{d}p_{\mathrm{T},2}} \mathrm{d}p_{\mathrm{T},2}}{\int_{0.32\times p_{\mathrm{T},1}}^{p_{\mathrm{T},1}} \frac{\mathrm{d}^2 N^{\mathrm{pair}}_{\mathrm{PYTHIA8}}(pp, 5.02 \text{ TeV})}{\mathrm{d}p_{\mathrm{T},1}\mathrm{d}p_{\mathrm{T},2}} \mathrm{d}p_{\mathrm{T},2}}. \tag{5}$$

Analogously, the ratio of pair nuclear-modification factors for subleading jets, $\rho_{\mathrm{Xe,Pb}}(p_{\mathrm{T},2})$, and the factor $C(p_{\mathrm{T},2})$ can be defined using Equation (4). The magnitude of the C factor ranges from 1.12 at 32 GeV to 1.31 at 398 GeV for both leading and sub-leading jets. The ratios $\rho_{\mathrm{Xe,Pb}}(p_{\mathrm{T},1})$ and $\rho_{\mathrm{Xe,Pb}}(p_{\mathrm{T},2})$ allow the differences between the jet quenching in Xe+Xe and Pb+Pb collisions to be directly quantified.

6 Systematic uncertainties

Systematic uncertainties arise from uncertainties in the JES, JER, background subtraction procedures, $\langle T_{\mathrm{AA}} \rangle$ values, the unfolding weight selection, minimum $p_{\mathrm{T},2}$ lower boundary, and from the unfolding procedure performance observed in the MC sample. For each source of systematic uncertainty, except for the uncertainty in $\langle T_{\mathrm{AA}} \rangle$ and unfolding non-closure, the entire analysis is repeated by varying the response matrix according to the systematic uncertainties. The difference between the final distributions of the baseline measurement and the measurement with varied values is used as the estimate of the systematic uncertainty. For the $\rho_{\mathrm{Xe,Pb}}$, the JES and JER systematic uncertainties are correlated between Xe+Xe and Pb+Pb, while all the other uncertainties are taken as uncorrelated.

The systematic uncertainty in the JES has four components. The first, centrality-independent component, is determined from in situ studies of the calorimeter response to jets reconstructed with the procedure used in 13 TeVpp collisions [21, 43]. The second component accounts for the relative energy-scale difference between the jet reconstruction procedures used in this analysis and those used for 13 TeVpp collisions [38]. The third component accounts for possible mis-modeling of the relative abundances of quark and gluon jets and the calorimeter response to them in the MC simulation. This is assessed by comparing quark and gluon jets generated with Pythia and with Herwig++. The fourth component is centrality dependent and accounts for any incomplete knowledge of the calorimetric response to quenched jets through modifications of parton showering [38, 44]. The total size of systematic uncertainty from the JES is approximately $1-8\%$ with the maximum around $x_{\mathrm{J}} \approx 0.32$ in $0-10\%$ central collisions. It decreases with x_{J} except for the last centrality interval where it increases, reaching a value of about 2%. For the $\rho_{\mathrm{Xe,Pb}}$, the largest systematic uncertainty from the JES is 5% and it exhibits only a weak p_{T} dependence.

The systematic uncertainty in the JER has two components. The first component is evaluated using an in situ technique for 13 TeV pp data that involves studies of dijet energy balance [45, 46]. The second component accounts for differences between the tower-based jet reconstruction and the jet reconstruction used in the analyses of 13 TeV pp data and the differences between the calibration procedures. Both of these uncertainties are applied via the smearing factor that is used to include an additional contribution to the resolution of the reconstructed p_{T} in the MC sample by the Gaussian smearing procedure. This modified reconstructed p_{T} enters the response matrices that are used to derive the alternative result. The uncertainty from the JER is approximately 10% for $x_{\mathrm{J}} \approx 0.32$ in 0–10% central collisions and decreases with x_{J} except for the last two intervals in x_{J} where it increases to about 5%. For $\rho_{\mathrm{Xe,Pb}}$, the largest systematic uncertainty from the JER is 2% and exhibits only a weak p_{T} dependence. The smaller JER uncertainty in $\rho_{\mathrm{Xe,Pb}}$ compared with the JES is due to a correlation with the Pb+Pb uncertainties.

The systematic uncertainty arising from the removal of the combinatoric jet background procedure has two components. The first component is connected with the determination of the yield of combinatoric background jets and is determined using an alternative sideband of $1.1 < \Delta\phi < 1.5$ following the procedure described in Ref. [12]. The second contribution is associated with the determination of the efficiency correction and is determined from the difference between the analysis performed with and without the efficiency correction. These uncertainties do not dominate the overall systematic uncertainty. The largest values of the uncertainty due to the determination of combinatoric jet background and the uncertainty due to the efficiency correction are about 1% and 2%, respectively, for both the x_{J} and $\rho_{\mathrm{Xe,Pb}}$ distributions.

The uncertainty in $\langle T_{\mathrm{AA}} \rangle$ arises from geometric modeling uncertainties (e.g. nucleon–nucleon inelastic cross-section, Woods–Saxon parameterization of the nucleon distribution [47, 48]) and the uncertainty of the fraction of selected inelastic Xe+Xe collisions. This uncertainty only affects the overall normalization

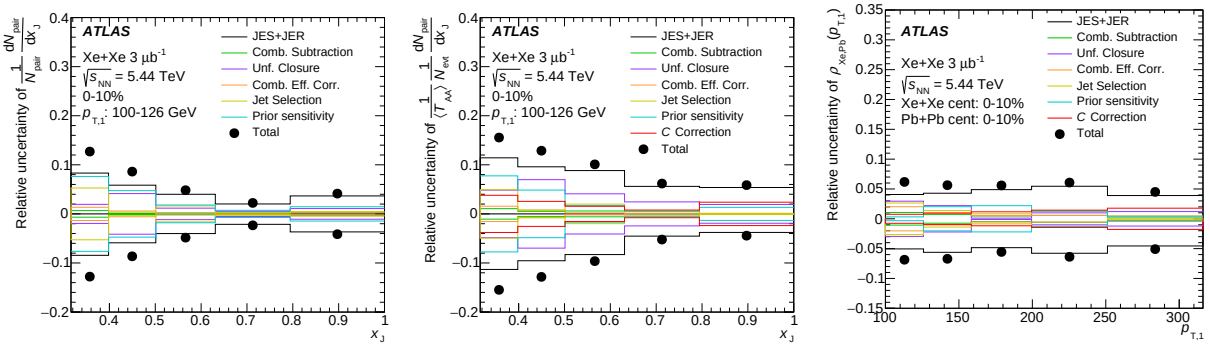

Figure 2: The relative magnitude of systematic uncertainties for (left) the per-pair normalized x_J distribution, (middle) the absolutely normalized x_J distribution, and (right) the $\rho_{Xe,Pb}(p_{T,1})$, all in the 0–10% centrality interval.

and is independent of the dijet kinematics. The values of the uncertainties in $\langle T_{AA}\rangle$ for Xe+Xe are shown in Table 1 and Table 2. This uncertainty is uncorrelated between Xe+Xe and Pb+Pb [13].

There are two sources of systematic uncertainty connected with the unfolding procedure. The first one arises from the imprecision in the determination of the initial distributions used in the iterative procedure for the underlying generator-level distribution in the unfolding procedure. This uncertainty is calculated from the difference between the unfolded distributions constructed using the nominal reweighted prior and the prior without applying the reweighting. The second source derives from the sensitivity of the unfolding procedure to the jet selection choice of the minimum jet p_T. This is estimated by changing the minimum jet p_T from 32 GeV to 25 GeV. To perform a check on the performance of the full analysis procedure a closure test is performed with the MC sample by evaluating the differences between the final unfolded distributions and the generator-level distributions of the MC sample. The difference from unity in the closure test is included as the additional source of systematic uncertainty. These uncertainties are the largest at low x_J, where the uncertainty due to the prior sensitivity reaches 10% for $100 < p_{T,1} < 126$ GeV in 0–10% central collisions. For larger x_J and p_T they decrease to 1–3%.

The uncertainty in the $C(p_T)$ factors defined in Section 5 is estimated as the difference between the $C(p_T)$ factors evaluated using PYTHIA 8 and HERWIG++ MC samples. The magnitude of the uncertainty in the C factor stays below 2% over the full p_T range of the $\rho_{Xe,Pb}$ distribution. The uncertainty in the $C(x_J)$ factor is evaluated in the same way as the uncertainty in the $C(p_T)$ factors. Its magnitude stays below 2%, and it is applied as the additional uncertainty in the Pb+Pb x_J distributions.

The magnitude of systematic uncertainties for per-pair normalized dijet momentum-imbalance, absolutely normalized dijet momentum-imbalance, and for the $\rho_{Xe,Pb}(p_{T,1})$ distributions, in the most central collisions, is shown in Figure 2.

7 Results

Figure 3 shows the per-pair normalized distribution of x_J evaluated in four centrality intervals (0–10%, 10–20%, 20–40%, and 40–80%) and three p_T intervals of the leading jet p_T ($100 < p_{T,1} < 126$ GeV, $126 < p_{T,1} < 158$ GeV, and $158 < p_{T,1} < 199$ GeV). A substantial difference between the shape of x_J distribution in the most central collisions (0–10%) and the most peripheral collisions (40–80%) is seen.

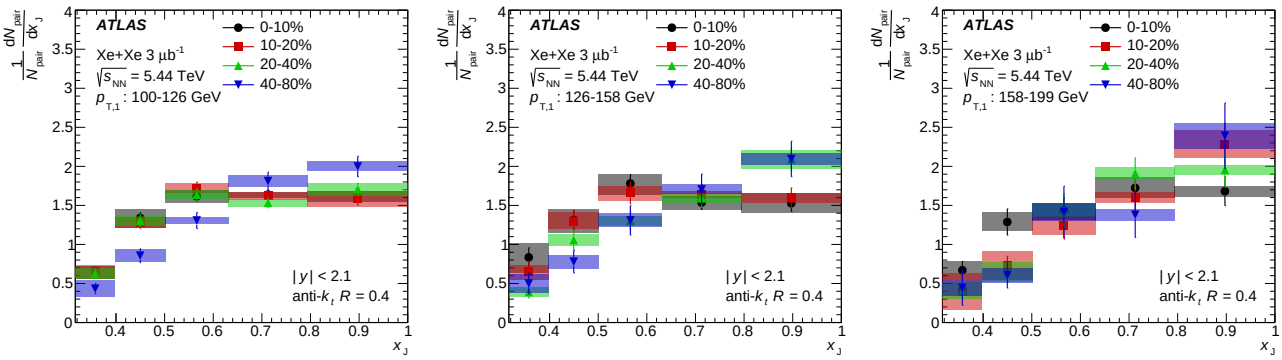

Figure 3: Per-pair normalized x_{J} distribution evaluated in four centrality intervals and three p_{T} intervals of leading jet p_{T}: (left) $100 < p_{\mathrm{T},1} < 126$ GeV, (middle) $126 < p_{\mathrm{T},1} < 158$ GeV, and (right) $158 < p_{\mathrm{T},1} < 199$ GeV. Statistical and systematic uncertainties are represented by error bars and boxes, respectively.

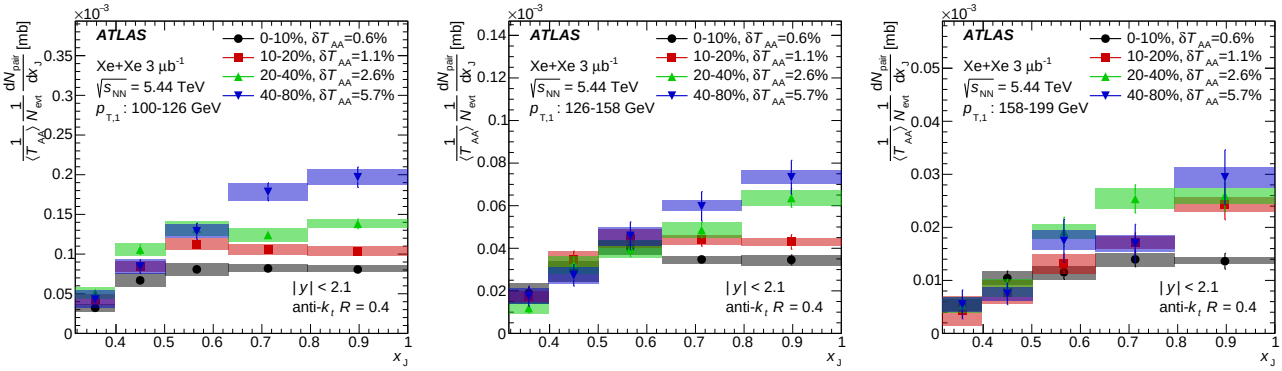

Figure 4: Absolutely normalized x_{J} distribution evaluated in four centrality intervals and three p_{T} intervals of leading jet p_{T}: (left) $100 < p_{\mathrm{T},1} < 126$ GeV, (middle) $126 < p_{\mathrm{T},1} < 158$ GeV, and (right) $158 < p_{\mathrm{T},1} < 199$ GeV. Statistical and systematic uncertainties are represented by error bars and boxes, respectively. The δT_{AA} in the legend represents the relative uncertainty on $\langle T_{\mathrm{AA}} \rangle$.

In peripheral collisions, the most frequent configurations are balanced dijets, while in central collisions the rate of imbalanced dijets is the same or higher than the rate of balanced dijets. Narrowing of the x_{J} distribution with increasing $p_{\mathrm{T},1}$ is also observed for all centrality intervals. These features are also observed in Pb+Pb collisions [13]. The peak structure at $x_{\mathrm{J}} = 0.6$ previously measured in 0–10% Pb+Pb collisions is however not present in 0–10% Xe+Xe collisions, which may be connected with a smaller overlapping region of colliding nuclei in Xe+Xe compared with Pb+Pb collisions. The evolution between the central and peripheral Xe+Xe collisions is not as pronounced as in Pb+Pb collisions. The absence of a clearly visible evolution is connected with a worse statistical precision of the Xe+Xe measurement compared with the Pb+Pb measurement.

Figure 4 shows the absolutely normalized distribution of x_{J} evaluated for the same centrality and $p_{\mathrm{T},1}$ selection as in Figure 3. It shows that the relative enhancement of imbalanced dijet topologies seen in Figure 3 is due to the depletion in the absolute yield of balanced dijets – an observation valid also in the Pb+Pb measurement. The results in Figure 4 show a clear centrality evolution where the suppression of the balanced dijet yield gradually decreases from central to peripheral collisions.

To compare the x_J distribution between Xe+Xe and Pb+Pb in an different way, the x_J distributions are evaluated in intervals of the same event activity, quantified by ΣE_T^{FCal}. The choice of ΣE_T^{FCal} intervals matches those measured in Pb+Pb for centrality intervals 10–20%, 20–40%, and 40–60%. The corresponding centrality intervals in Xe+Xe collisions are given in Table 2. The most central Pb+Pb interval (0–10%) cannot be used since the equivalent event activity is not present in Xe+Xe collisions. The Xe+Xe to Pb+Pb comparison of per-pair normalized x_J distributions is presented in Figure 5 in the $100 < p_{T,1} < 126$ GeV interval. The distributions measured within the same event activity interval are consistent between Xe+Xe and Pb+Pb collisions. A similar agreement is also found in other $p_{T,1}$ selections. The smaller systematic uncertainties for the lower statistic Xe+Xe collisions are connected with the coarser binning used in Xe+Xe data, which results in smaller bin-to-bin migrations and, consequently, smaller systematic uncertainties related to the unfolding procedure.

The comparison of absolutely normalized x_J distributions between Pb+Pb and Xe+Xe in the same event activity intervals is presented in the upper plots of Figure 6. A clear difference between Xe+Xe and Pb+Pb distributions can be seen, with Xe+Xe having a larger absolute yield than Pb+Pb. This difference may be partially attributed to the difference between the hard process cross-sections, due to the different center-of-mass energies of the initial hard scattering, in Xe+Xe and Pb+Pb collisions. To estimate the impact of the difference between the center-of-mass energies, the absolutely normalized x_J distributions in Pb+Pb collisions are scaled by $C(x_J)$ defined in Equation (3). The result is shown in the bottom plots of Figure 6. After correcting for the difference between the center-of-mass energies of the initial hard scattering, the absolutely normalized x_J distributions agree between Xe+Xe and Pb+Pb collisions within uncertainties. The same conclusion is also found for other $p_{T,1}$ intervals. While the observed agreement could arise from canceling effects and large uncertainties, a natural explanation for this behavior is that the difference between the energies of the hard scattering process plays a significant role in the absolutely normalized x_J distributions.

In the case of per-pair normalized x_J distributions, the correction factor $C(x_J)$ was found to be consistent with unity, which is consistent with observing an agreement of per-pair normalized x_J distributions between Xe+Xe and Pb+Pb collisions.

To characterize the differences between Xe+Xe and Pb+Pb dijet suppression in a more quantitative way, the Xe+Xe to Pb+Pb ratio of pair nuclear-modification factors, $\rho_{Xe,Pb}$, are evaluated as defined in Section 5. The $\rho_{Xe,Pb}(p_{T,1})$ and $\rho_{Xe,Pb}(p_{T,2})$ evaluated in the same Xe+Xe and Pb+Pb centrality intervals are shown in Figure 7. The $\rho_{Xe,Pb}$ values obtained are systematically larger than unity, typically by 10% to 20% depending on centrality. Figure 8 shows $\rho_{Xe,Pb}$ evaluated in the same event activity intervals. In contrast to the centrality-based comparison, the $\rho_{Xe,Pb}$ values are consistent with unity within statistical and systematic uncertainties. This implies that the pair nuclear-modification factor in Xe+Xe collisions at $\sqrt{s_{NN}} = 5.44$ TeV is consistent with the same quantity measured at $\sqrt{s_{NN}} = 5.02$ TeV in Pb+Pb collisions which suggests that the suppression of dijets does not differ in a significant way between Xe+Xe and Pb+Pb collisions when measured in the same event activity intervals.

Despite consistency of $\rho_{Xe,Pb}$ with the unity, we should still emphasize that any interpretation of the difference between the pair R_{AA} evaluated as a function of $p_{T,1}$ and $p_{T,2}$ as the difference between the overall suppression of leading and subleading jets needs to take into account that the yields entering the pair R_{AA} are conditional yields mutually dependent on kinematic selection criteria. Consequently, any interpretation of $\rho_{Xe,Pb}(p_{T,1})$, $\rho_{Xe,Pb}(p_{T,2})$ and $R_{AA}^{pair}(p_{T,1})$, $R_{AA}^{pair}(p_{T,2})$ must be performed in the context of theoretical model predictions that directly follow the dijet definition and projection procedures used in this analysis.

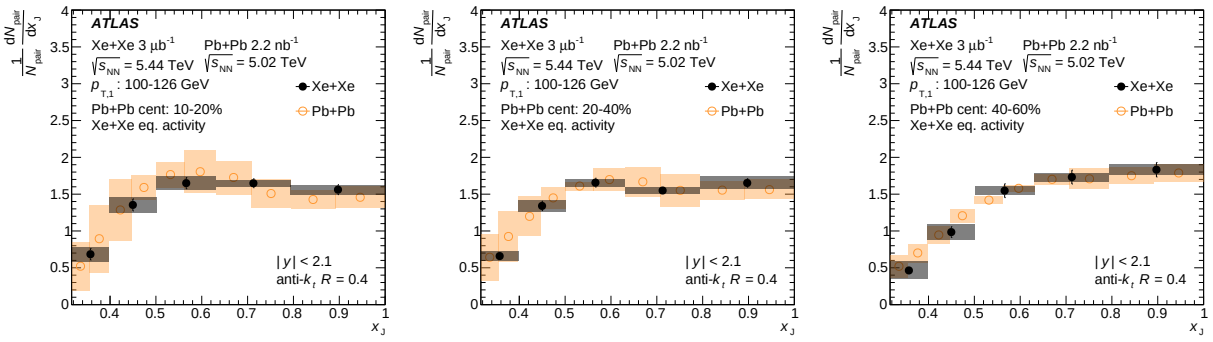

Figure 5: Comparison of Xe+Xe (filled points) and Pb+Pb (open points) per-pair normalized x_J distributions in $100 < p_{T,1} < 126$ GeV and 10–20%, 20–40%, and 40–60% Pb+Pb centrality intervals and in the corresponding Xe+Xe ΣE_T^{FCal} intervals. Statistical and systematic uncertainties are represented by error bars and boxes, respectively.

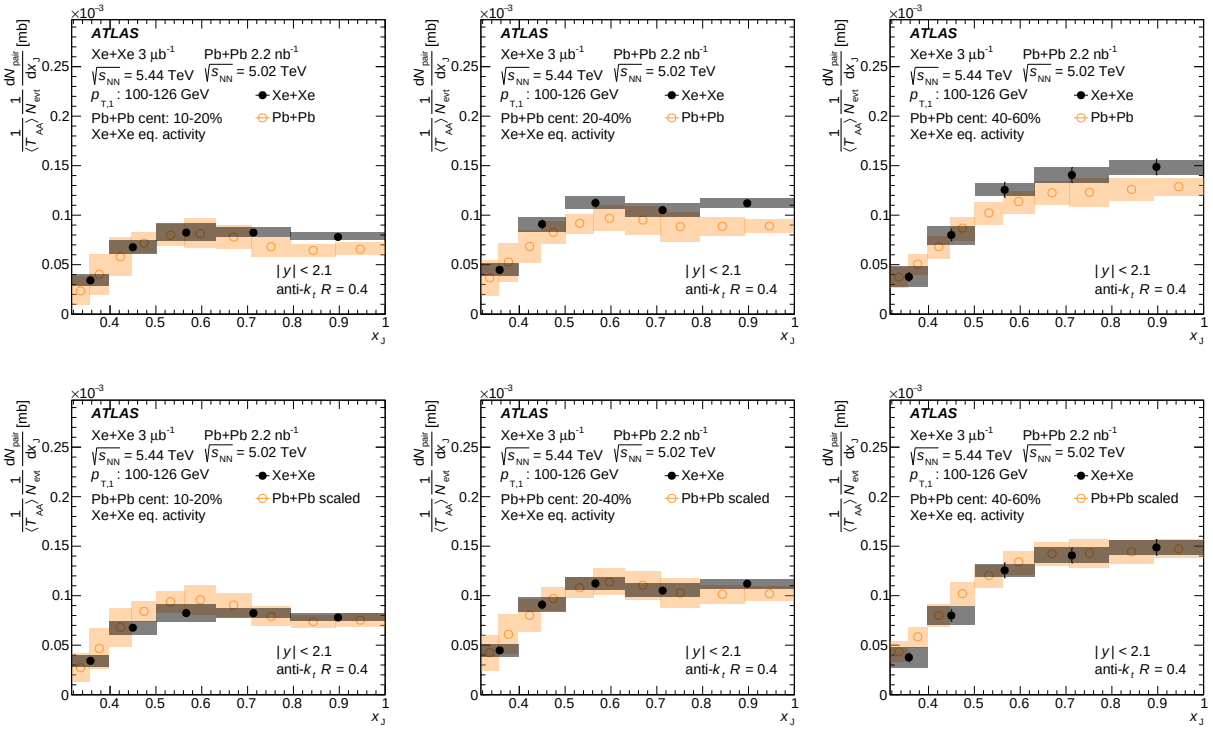

Figure 6: Comparison of Xe+Xe (filled points) and Pb+Pb (open points) absolutely normalized x_J distributions in $100 < p_{T,1} < 126$ GeV and 10–20%, 20–40%, and 40–60% Pb+Pb centrality intervals and in the corresponding Xe+Xe ΣE_T^{FCal} intervals. The upper plots show directly measured distributions. The lower plots show the Pb+Pb distributions corrected for the impact of the difference between the center-of-mass energies of the hard scattering process in Xe+Xe and Pb+Pb collisions. Statistical and systematic uncertainties are represented by error bars and boxes, respectively.

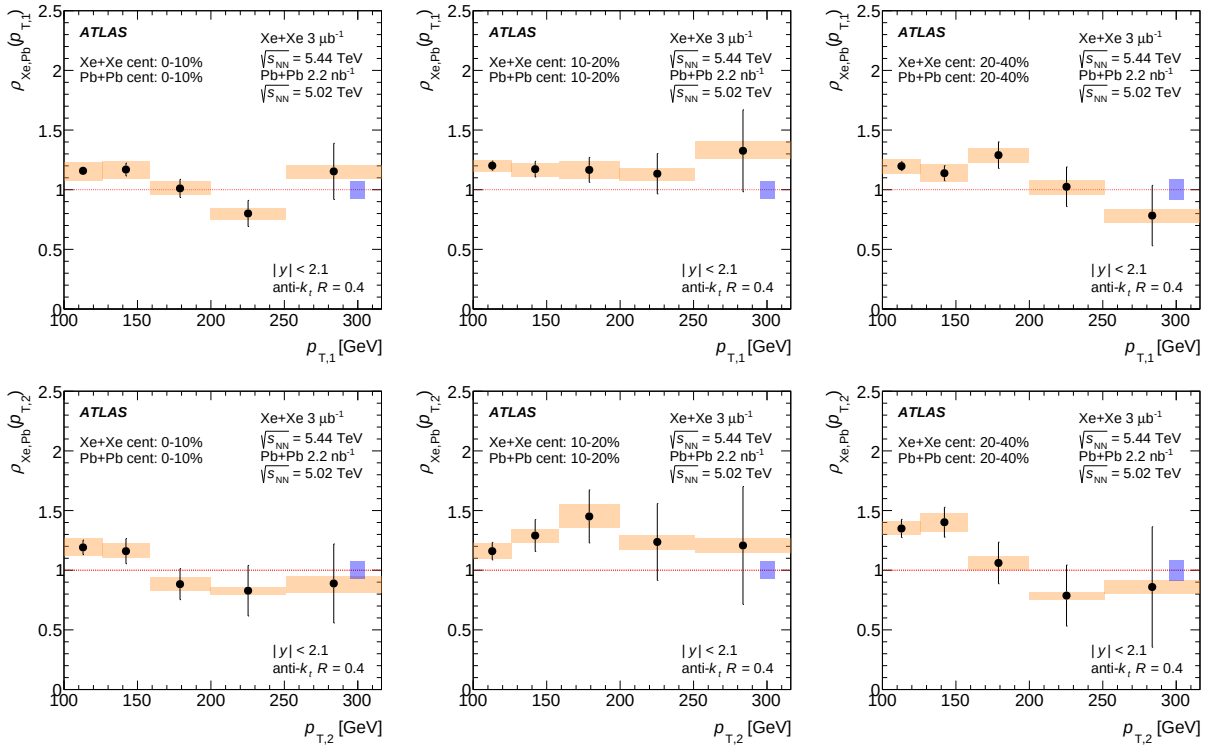

Figure 7: The ratios of Xe+Xe and Pb+Pb pair nuclear-modification factors, $\rho_{\mathrm{Xe,Pb}}$, evaluated as a function of (upper plots) $p_{\mathrm{T},1}$ and (lower plots) $p_{\mathrm{T},2}$ in the same centrality intervals. Statistical and systematic uncertainties are represented by error bars and boxes, respectively. The box centered at unity represents the fractional systematic uncertainty on $\langle T_{\mathrm{AA}} \rangle$.

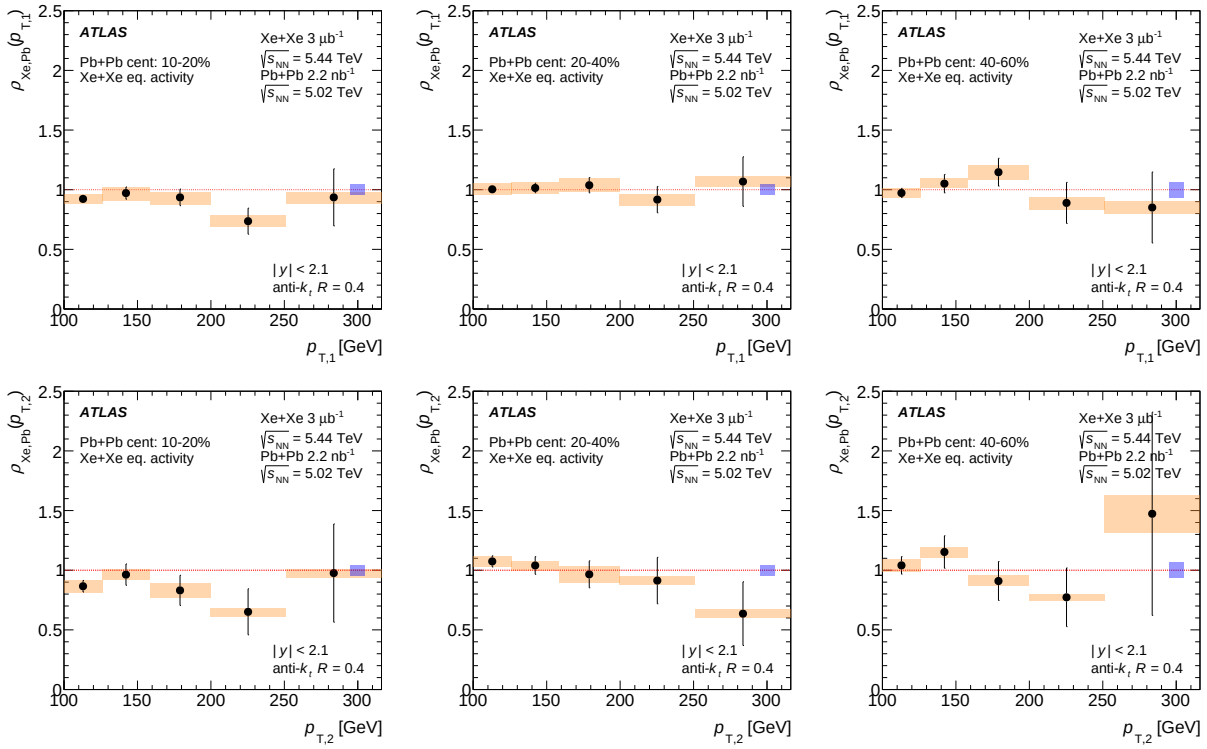

Figure 8: The ratios of Xe+Xe and Pb+Pb pair nuclear-modification factors, $\rho_{\mathrm{Xe,Pb}}$, evaluated as a function of (upper plots) $p_{\mathrm{T},1}$ and (lower plots) $p_{\mathrm{T},2}$ in the same $\Sigma E_{\mathrm{T}}^{\mathrm{FCal}}$ intervals (selecting equivalent event activity). Statistical and systematic uncertainties are represented by error bars and boxes, respectively. The box centered at unity represents the fractional systematic uncertainty on $\langle T_{\mathrm{AA}} \rangle$.

8 Conclusions

A measurement of per-pair normalized and absolutely normalized x_J distributions of dijets in Xe+Xe collisions at $\sqrt{s_{NN}} = 5.44$ TeV using 3 μb^{-1} of data collected with the ATLAS detector at the LHC is presented. The per-pair normalized x_J distributions indicate a higher relative rate of imbalanced dijets in central Xe+Xe collisions compared with peripheral ones. The absolutely normalized x_J distributions show that this feature arises predominantly from a depletion of the yields of more balanced dijets with x_J values close to unity.

The results are compared with a measurement of dijets in Pb+Pb collisions at $\sqrt{s_{NN}} = 5.02$ TeV by ATLAS. The x_J distributions are found to be consistent between Pb+Pb and Xe+Xe collisions when compared in the same event activity intervals and after correcting the absolutely normalized distributions for the expected difference between the hard process cross-sections due to the different center-of-mass energies between Xe+Xe and Pb+Pb collisions. Furthermore, the differences between the dijet suppression in Xe+Xe and Pb+Pb are quantified by the ratio of pair nuclear-modification factors, $\rho_{Xe,Pb}$, which are found to be consistent with unity when evaluated in the same event activity intervals.

These results should provide input for a better understanding of the role of path length, energy density, and fluctuations in the jet-energy loss in the QGP and add a new input to the quantification of its system size dependence.

References

[1] G.-Y. Qin and X.-N. Wang, *Jet quenching in high-energy heavy-ion collisions*, Int. J. Mod. Phys. E **24** (2015) 1530014, arXiv: 1511.00790 [hep-ph].

[2] J.-P. Blaizot and Y. Mehtar-Tani, *Jet structure in heavy ion collisions*, Int. J. Mod. Phys. E **24** (2015) 1530012, arXiv: 1503.05958 [hep-ph].

[3] L. Cunqueiro and A. M. Sickles, *Studying the QGP with Jets at the LHC and RHIC*, Prog. Part. Nucl. Phys. **124** (2022) 103940, arXiv: 2110.14490 [nucl-ex].

[4] ATLAS Collaboration, *Measurement of the nuclear modification factor for inclusive jets in Pb+Pb collisions at* $\sqrt{s_{NN}} = 5.02$ *TeV with the ATLAS detector*, Phys. Lett. B **790** (2019) 108, arXiv: 1805.05635 [hep-ex].

[5] CMS Collaboration, *Measurement of inclusive jet cross-sections in pp and PbPb collisions at* $\sqrt{s_{NN}} = 2.76$ *TeV*, Phys. Rev. C **96** (2017) 015202, arXiv: 1609.05383 [hep-ex].

[6] ALICE Collaboration, *Measurements of inclusive jet spectra in pp and central Pb-Pb collisions at* $\sqrt{s_{\mathrm{NN}}} = 5.02$ *TeV*, Phys. Rev. C **101** (2020) 034911, arXiv: 1909.09718 [nucl-ex].

[7] G.-Y. Qin and B. Müller, *Explanation of Di-jet asymmetry in Pb+Pb collisions at the Large Hadron Collider*, Phys. Rev. Lett. **106** (2011) 162302, [Erratum: Phys. Rev. Lett. **108**, 189904 (2012)], arXiv: 1012.5280 [hep-ph].

[8] J. G. Milhano and K. C. Zapp, *Origins of the di-jet asymmetry in heavy ion collisions*, Eur. Phys. J. C **76** (2016) 288, arXiv: 1512.08107 [hep-ph].

[9] ATLAS Collaboration, *Observation of a Centrality-Dependent Dijet Asymmetry in Lead–Lead Collisions at* $\sqrt{s_{NN}} = 2.76$ *TeV with the ATLAS Detector at the LHC*, Phys. Rev. Lett. **105** (2010) 252303, arXiv: 1011.6182 [hep-ex].

[10] CMS Collaboration, *Observation and studies of jet quenching in PbPb collisions at* $\sqrt{s_{NN}} = 2.76$ *TeV*, Phys. Rev. C **84** (2011) 024906, arXiv: 1102.1957 [hep-ex].

[11] CMS Collaboration, *Jet momentum dependence of jet quenching in PbPb collisions at* $\sqrt{s_{NN}} = 2.76$ *TeV*, Phys. Lett. B **712** (2012) 176, arXiv: 1202.5022 [hep-ex].

[12] ATLAS Collaboration, *Measurement of jet* p_T *correlations in Pb+Pb and pp collisions at* $\sqrt{s_{NN}} = 2.76$ *TeV with the ATLAS detector*, Phys. Lett. B **774** (2017) 379, arXiv: 1706.09363 [hep-ex].

[13] ATLAS Collaboration, *Measurements of the suppression and correlations of dijets in Pb+Pb collisions at* $\sqrt{s_{NN}} = 5.02$ *TeV*, (2022), arXiv: 2205.00682 [nucl-ex].

[14] ATLAS Collaboration, *Charged-hadron production in pp, p+Pb, Pb+Pb, and Xe+Xe collisions at* $\sqrt{s_{NN}} = 5$ *TeV with the ATLAS detector at the LHC*, (2022), arXiv: 2211.15257 [hep-ex].

[15] CMS Collaboration, *Charged-particle nuclear modification factors in XeXe collisions at* $\sqrt{s_{NN}} = 5.44$ *TeV*, JHEP **10** (2018) 138, arXiv: 1809.00201 [hep-ex].

[16] ALICE Collaboration, *Transverse momentum spectra and nuclear modification factors of charged particles in Xe-Xe collisions at* $\sqrt{s_{NN}} = 5.44$ *TeV*, Phys. Lett. B **788** (2019) 166, arXiv: 1805.04399 [nucl-ex].

[17] Z. Citron et al., *Report from Working Group 5: Future physics opportunities for high-density QCD at the LHC with heavy-ion and proton beams*, CERN Yellow Rep. Monogr. **7** (2019) 1159, ed. by A. Dainese et al., arXiv: 1812.06772 [hep-ph].

[18] ATLAS Collaboration, *The ATLAS Experiment at the CERN Large Hadron Collider*, JINST **3** (2008) S08003.

[19] ATLAS Collaboration, *Performance of the ATLAS trigger system in 2015*, Eur. Phys. J. C **77** (2017) 317, arXiv: 1611.09661 [hep-ex].

[20] ATLAS Collaboration, *The ATLAS Collaboration Software and Firmware*, ATL-SOFT-PUB-2021-001, 2021, URL: https://cds.cern.ch/record/2767187.

[21] ATLAS Collaboration, *Jet energy measurement with the ATLAS detector in proton–proton collisions at* $\sqrt{s} = 7$ *TeV*, Eur. Phys. J. C **73** (2013) 2304, arXiv: 1112.6426 [hep-ex].

[22] C. Loizides, J. Kamin, and D. d'Enterria, *Improved Monte Carlo Glauber predictions at present and future nuclear colliders*, Phys. Rev. C **97** (2018) 054910, [Erratum: Phys.Rev.C **99**, 019901 (2019)], arXiv: 1710.07098 [nucl-ex].

[23] ATLAS Collaboration, *Measurement of the azimuthal anisotropy for charged particle production in* $\sqrt{s_{NN}} = 2.76$ *TeV lead–lead collisions with the ATLAS detector*, Phys. Rev. C **86** (2012) 014907, arXiv: 1203.3087 [hep-ex].

[24] ATLAS Collaboration, *Measurement of the pseudorapidity and transverse momentum dependence of the elliptic flow of charged particles in lead–lead collisions at* $\sqrt{s_{NN}} = 2.76$ *TeV with the ATLAS detector*, Phys. Lett. B **707** (2012) 330, arXiv: 1108.6018 [hep-ex].

[25] T. Sjöstrand et al., *An introduction to PYTHIA 8.2*, Comput. Phys. Commun. **191** (2015) 159, arXiv: 1410.3012 [hep-ph].

[26] ATLAS Collaboration, *ATLAS Pythia 8 tunes to 7 TeV data*, ATL-PHYS-PUB-2014-021, 2014, URL: https://cds.cern.ch/record/1966419.

[27] R. D. Ball et al., *Parton distributions with LHC data*, Nucl. Phys. B **867** (2013) 244, arXiv: 1207.1303 [hep-ph].

[28] GEANT4 Collaboration, S. Agostinelli, et al., *GEANT4 – a simulation toolkit*, Nucl. Instrum. Meth. A **506** (2003) 250.

[29] ATLAS Collaboration, *The ATLAS Simulation Infrastructure*, Eur. Phys. J. C **70** (2010) 823, arXiv: 1005.4568 [physics.ins-det].

[30] M. Bähr et al., *Herwig++ physics and manual*, Eur. Phys. J. C **58** (2008) 639, arXiv: 0803.0883 [hep-ph].

[31] S. Gieseke, C. Rohr, and A. Siodmok, *Colour reconnections in Herwig++*, Eur. Phys. J. C **72** (2012) 2225, arXiv: 1206.0041 [hep-ph].

[32] J. Pumplin et al.,
New Generation of Parton Distributions with Uncertainties from Global QCD Analysis,
JHEP **07** (2002) 012, arXiv: hep-ph/0201195.

[33] ATLAS Collaboration, *Measurements of azimuthal anisotropies of jet production in Pb+Pb collisions at* $\sqrt{s_{NN}} = 5.02$ *TeV with the ATLAS detector*, Phys. Rev. C **105** (2021) 064903, arXiv: 2111.06606 [nucl-ex].

[34] M. Cacciari, G. P. Salam, and G. Soyez, *The anti-k_t jet clustering algorithm*, JHEP **04** (2008) 063, arXiv: 0802.1189 [hep-ph].

[35] M. Cacciari, G. P. Salam, and G. Soyez, *FastJet user manual*, Eur. Phys. J. C **72** (2012) 1896, arXiv: 1111.6097 [hep-ph].

[36] ATLAS Collaboration, *Measurement of the azimuthal anisotropy of charged particles produced in* $\sqrt{s_{NN}} = 5.02$ *TeV Pb+Pb collisions with the ATLAS detector*, Eur. Phys. J. C **78** (2018) 997, arXiv: 1808.03951 [hep-ex].

[37] ATLAS Collaboration, *Jet energy measurement and its systematic uncertainty in proton–proton collisions at* $\sqrt{s} = 7$ *TeV with the ATLAS detector*, Eur. Phys. J. C **75** (2015) 17, arXiv: 1406.0076 [hep-ex].

[38] ATLAS Collaboration,
Jet energy scale and its uncertainty for jets reconstructed using the ATLAS heavy ion jet algorithm,
ATLAS-CONF-2015-016, 2015, URL: https://cds.cern.ch/record/2008677.

[39] ATLAS Collaboration, *Measurement of photon-jet transverse momentum correlations in* 5.02 *TeV Pb+Pb and pp collisions with ATLAS*, Phys. Lett. B **789** (2019) 167, arXiv: 1809.07280 [hep-ex].

[40] ATLAS Collaboration, *Measurement of the jet radius and transverse momentum dependence of inclusive jet suppression in lead–lead collisions at* $\sqrt{s_{NN}} = 2.76$ *TeV with the ATLAS detector*, Phys. Lett. B **719** (2013) 220, arXiv: 1208.1967 [hep-ex].

[41] T. Adye, "Unfolding algorithms and tests using RooUnfold,"
Proceedings, 2011 Workshop on Statistical Issues Related to Discovery Claims in Search Experiments and Unfolding (PHYSTAT 2011) (CERN, Geneva, Switzerland, Jan. 17–20, 2011) 313, arXiv: 1105.1160 [physics.data-an].

[42] G. D'Agostini, *A multidimensional unfolding method based on Bayes' theorem*,
Nucl. Instrum. Meth. A **362** (1995) 487.

[43] ATLAS Collaboration, *Jet energy scale measurements and their systematic uncertainties in proton–proton collisions at* $\sqrt{s} = 13$ *TeV with the ATLAS detector*, Phys. Rev. D **96** (2017) 072002, arXiv: 1703.09665 [hep-ex].

[44] ATLAS Collaboration, *Measurements of the Nuclear Modification Factor for Jets in Pb+Pb Collisions at* $\sqrt{s_{NN}} = 2.76$ *TeV with the ATLAS Detector*, Phys. Rev. Lett. **114** (2015) 072302, arXiv: 1411.2357 [hep-ex].

[45] ATLAS Collaboration, *Determination of jet calibration and energy resolution in proton–proton collisions at* $\sqrt{s} = 8$ *TeV using the ATLAS detector*, Eur. Phys. J. C **80** (2020) 1104, arXiv: 1910.04482 [hep-ex].

[46] ATLAS Collaboration, *Jet energy resolution in proton–proton collisions at* $\sqrt{s} = 7$ *TeV recorded in 2010 with the ATLAS detector*, Eur. Phys. J. C **73** (2013) 2306, arXiv: 1210.6210 [hep-ex].

[47] M. L. Miller, K. Reygers, S. J. Sanders, and P. Steinberg,
Glauber Modeling in High-Energy Nuclear Collisions, Ann. Rev. Nucl. Part. Sci. **57** (2007) 205, arXiv: nucl-ex/0701025.

[48] D. d'Enterria and C. Loizides, *Progress in the Glauber Model at Collider Energies*, Ann. Rev. Nucl. Part. Sci. **71** (2021) 315, arXiv: 2011.14909 [hep-ph].